Simulating orientation and polarization characteristics of dense fibrous tissue by electrostatic spinning of polymeric fibers

SHUWEI SHEN,[1] HAILI WANG,[1] YINGJIE QU,[1] KUIMING HUANG,[1] GUANGLI LIU,[1] ZEXIN CHEN,[1] CANZHEN MA,[1] PENGFEI SHAO,[1] JIN HONG,[2] PAUL LEMAILLET,[3] ERBAO DONG,[1] AND RONALD X. XU[1,4,*]

[1]Department of Precision Machinery and Precision Instrumentation, University of Science and Technology of China, Hefei 230026, China
[2]Key Laboratory of Environmental Optics and Technology, Anhui Institute of Optics and Fine Mechanics, Chinese Academy of Sciences, Hefei 230031, China
[3]National Institute of Standards and Technology, 100 Bureau Drive, Gaithersburg, MD 20899, USA
[4]Department of Biomedical Engineering, The Ohio State University, Columbus, OH 43210, USA
*xu.ronald@hotmail.com

Abstract: Phantoms simulating polarization characteristics of soft tissue play an important role in the development, calibration, and validation of diagnostic polarized imaging devices and of therapeutic strategy, in both laboratory and clinical settings. We propose to fabricate optical phantoms that simulate polarization characteristics of dense fibrous tissues by bonding electrospun polylactic acid (PLA) fibers between polydimethylsiloxane (PDMS) substrate with a groove. Increasing the rotational speed of an electrospinning collector helps improve the orientation of the electrospun fibers. The phantoms simulate the polarization characteristics of dense fibrous tissue of collagenous fibroma and healthy skin with high fidelity. Our experiments demonstrate the technical potential of using such phantoms for validation and calibration of polarimetric medical devices.

1. Introduction

The human skin is the largest organ of the integumentary system and plays an important role in protecting against pathogens and excessive water loss [1]. However, lesions or mechanical damages seriously threaten health by breaking the circulations associated with dermal structure and composition [2]. Especially, soft-tissue tumors, such as frequently occurring fibromas, disrupt the regular structure and composition of fibrous tissues [3]. Therefore, accurate detection of fibrous tissue anomalies may facilitate more effective diagnosis and treatment of various tissue malignancies. Optical imaging is part of family of low-cost and portable technologies for non-invasive detection of tissue anomalies [4]. The emergence of collagen-sensitive polarized light imaging technique allows for accurate detection of polarization characteristics induced by birefringent anomalies in lesion-like fibrous tissue [5,6]. Other polarization-based techniques, such as polarized light dermoscopy, hand-held polarimeter and polarization sensitive-optical coherence tomography, have also demonstrated the clinical utility for disease detection and guided therapy [7,8]. Optical imaging devices need regular calibration to reduce measurement deviation and facilitate reliable detection of tissue parameters. Optical phantoms that simulate tissue scattering and absorption properties have been designed and fabricated for verification and calibration of various optical imaging modalities, such as diffuse optical imaging, spectroscopy, and confocal microscopy [9,10]. Phantoms that simulate the structural heterogeneity of biologic tissue have also been developed for surgical navigation and therapeutic validation [11,12].

To calibrate polarized light imaging devices, optical phantoms that simulate polarization characteristics of biologic tissue have also been developed using various materials. For

example, a commercially available Collagen Hemostatic Sponge composed almost exclusively of type I collagen has been applied to verify parameters of polarization sensitive optical coherence tomography (PS-OCT) [13]. Rubber phantoms of controllable birefringence induced by different degrees of stretch are also reported for verification of polarized imaging device [14]. Other researchers have developed a relatively stable phantom with adjustable birefringence by dispersing ellipsoidal melanin particles in an isotropic liquid media [15]. However, the softness and fixed-birefringence of type I collagen phantoms, the relaxation of stress resulting in a birefringence decay of the rubber phantoms, and the difficulty of long-term preservation of the liquid phantoms have prevented the promotion of these types of phantoms as traceable standards for medical optical imaging. Therefore, it is necessary to develop a birefringent phantom with longer shelf life and controllable parameters.

An emerging process of electrospinning allows for reproducible production of polymeric fibers with controllable size range from several nanometers to a few micrometers by drawing electrically charged threads of polymer solutions in an elevated electric field [16,17]. The process has gained broad applications in many fields such as environmental remediation, energy research, drug delivery, and tissue engineering [18,19]. By adjusting the process parameters, it is possible to generate electrospun fibers with desired geometric structures, alignment directions, and crystalline orientations [20–22]. Since crystalline orientation contributes to birefringence [23], controlling the fiber drawing speed in electrospinning allows us to simulate the birefringence characteristics of biologic tissue [23,24]. Since fiber orientation contributes to the polarization, controlling the rotational speed of the cylindrical collector allows us to produce electrospun fibers of high alignment uniformity to simulate the polarization properties of biologic tissue [25]. Experimentally, electrospun fibers have been used to construct phantoms for validation of polarized spatial frequency domain imaging and diffusion magnetic resonance imaging [26,27].

This paper introduces a novel optical phantom that simulates tissue polarization properties by controlled alignment of electrospun polylactic acid (PLA) fibers with a diameter from 1 µm to 2.2 µm and with different fiber orientations. The produced solid phantoms can simulate the polarization characteristics of both dense fibrous tissue of collagenous fibroma and healthy skin. Such a polarization-mimicking phantom can be used for calibrating polarimetric medical devices and for studying fibrous tissue anomalies.

2. Materials and methods

2.1 Materials

PLA (17wt %, Mw≈100,000 g/mole, Shanghai Civi Chemical Technology Co., Ltd, Shanghai, China) was dissolved in a mixture of chloroform and acetone (2:1 volume ratio) [28,29]. Conductive aluminum foil (Chong Fung soft membrane Co., Ltd, Shantou, China) was used to collect the electrospun fibers. Optically clear and non-toxic polydimethylsiloxane (PDMS, Sylgard® 184, Dow Corning Corp., Midland, MI, USA) was used as the base material for phantom construction [30]. Biopsy samples of collagenous fibroma and healthy skin (thickness: 4~6 µm) were obtained from Hongye Teaching Instrument Co., Ltd (Xinxiang, China). These samples were dewaxed with xylene before characterization of polarization properties in comparison with those of tissue-simulating phantoms.

2.2 Electrospinning device for fabricating PLA fibers

Figure 1(a) shows the schematic diagram and the experimental setup of the electrospinning process. As a static electrical field is applied between the nozzle and the ground target, a charged jet of polymer solution is ejected when the applied electric field overcomes the surface tension of the droplet [31]. Due to the chaotic oscillation of the electrospinning jet, the electrospinning process generates randomly oriented fibers unless a special collection device is used [32]. A rotating cylindrical collector with a diameter of 7.5 cm (Foshan leptons

Precision Measurement and Control Technology Co., Ltd, China) was used to collect the fibers and a metal dispensing head of 0.8 mm in diameter was used as the nozzle (Fig. 1(c)).
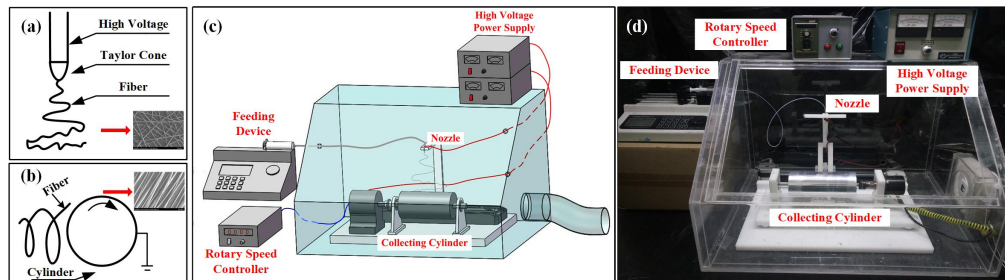

Fig. 1. Electrospinning system. (a) Principle of the electrospinning process. (b) Schematic diagram of the process of collecting fibers (c) CAD design of the electrospinning system. (d) Experimental setup of the electrospinning system.

The size and surface characteristics of the electrospun fibers are affected by both the properties of polymer solution and the parameters of the fabrication process. As the concentration of the polymer solution increases, the viscosity increases and the resultant fiber diameter increases [33]. The process produces droplets and beads instead of fibers as the viscosity of polymer solution decreases [34,35]. On the other hand, as the applied voltage increases, more fluid is ejected from the nozzle, resulting in fibers of larger diameter and rougher surface finish [36]. Meanwhile, the distance between the collector and the nozzle needs to vary with the polymer solution concentration to allow sufficient time of fly for solvent evaporation. After experimenting with different fabrication process parameters, we have defined the following set of electrospinning parameters: a feed rate of 0.8 ml/h, supplied voltages of 8 kilovolts for the nozzle and 0 kilovolt for the collector, and a collector-to-nozzle distance of 8 cm. By applying the above process parameters, we were able to produce the electrospun fibers with the desired birefringence characteristics at room temperature of 28° and humidity around 50%. By collecting PLA fibers on a rotating cylinder at a rotational speed ranging from 0 revolutions per minute (rpm) to 3000 rpm in steps of 500 rpm, we were able to produce fibers of controlled polarization characteristics

2.3 Polarized light detection system

As shown in Fig. 2, the polarization measurement setup consists of a light source, a polarizer, a sample stage, an analyzer, and a charge-coupled device (CCD) camera. As linearly polarized light at the output of the polarizer is incident to a linearly birefringent sample, the intensity of transmitted light varies with the angular orientation of the sample [37]. When the analyzer and the polarizer are cross-polarized, the CCD camera can detect the transmitted light when the sample orientation parameter β (i.e., the angle between the polarizer and the fast polarization axis of the sample) is not zero
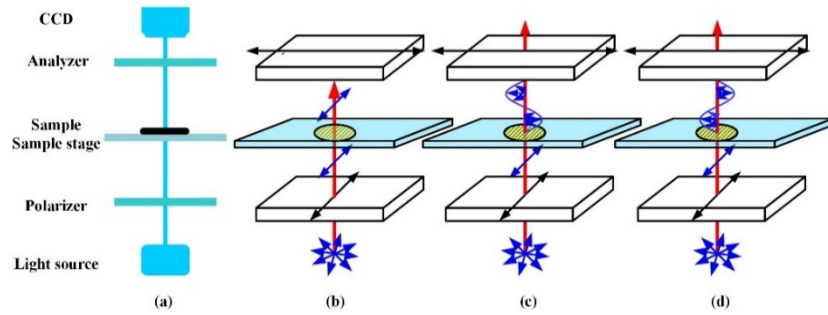
Fig. 2. Overview of the polarized detection system in orthogonal mode. (a) Schematic diagram of the polarized detection system. (b-d) The analyzer and the polarizer are cross-polarized in the orthogonal mode, and the polarized light detected by the CCD camera is dependent of β the angle between the fast polarization axis of the sample and the polarizer. Here the polarizer is fixed and the analyzer is rotated to switch between the orthogonal and the perpendicular modes.

With the direction of the polarizer parallel to the X axis, the stokes vector of the detected light can be expressed as [38]:

$$\vec{s_2} = \mathbf{M}_2 \mathbf{M}_p \mathbf{M}_1 \vec{s_1} = \frac{I_0}{2} \begin{bmatrix} \sin^2 2\beta \sin^2 \dfrac{\sigma}{2} \\ \sin^2 2\beta \sin^2 \dfrac{\sigma}{2} \\ 0 \\ 0 \end{bmatrix} \tag{1}$$

where I_0 is the intensity of the light source; σ is the sample-induced phase retardation, $\vec{s_1}$ is the incident Stokes vector and $\vec{s_2}$ is the Stokes vector at the output of the analyzer. $\mathbf{M}_1$, $\mathbf{M}_2$ and $\mathbf{M}_P$ are the Mueller matrices of the polarizer, the analyzer and the linear birefringent element, respectively. The sample-induced phase retardation σ is further expressed as $2\pi d \triangle n/\lambda$ [39], where λ is the wavelength, d the thickness of the sample, $\triangle n$ the sample birefringence, and I_1 the light intensity passing through the parallel analyzer and polarizer ($I_1 = I_0/2$) [40]. The intensity of the light at the output of the analyzer is [41]:

$$I = I_1 \sin^2 2\beta \sin^2 \frac{\pi d \triangle n}{\lambda} \tag{2}$$

In the orthogonal mode, for an isotropic sample presenting no birefringence, no light is detected regardless the rotational angle of the sample. For an anisotropic sample with single distribution of orientation, the transmitted light through the sample can be linearly, elliptically or circularly polarized [42]. Consequently, the intensity of the light detected by the CCD camera varies periodically with the change of the sample angular orientation.

3. Results

3.1 Electrospinning of PLA fibers

PLA fibers were produced by electrospinning under different fabrication process conditions. The orientation of the produced fibers aligns more uniformly when the rotational speed of the collection cylinder increases. As the speed of fiber collection approximates the speed of fiber generation, PLA fibers with a single distribution of orientation can be collected [33]. In our experiment, PLA samples of the identical thickness were produced by electrospinning at the same feeding rate, the same collection time (7 min), but different rotational speeds of the

cylindrical collector. The electrospun fibers were collected by the aluminum foil on the surface of the cylindrical collector and cut into blocks of 3cmx3cm for further testing and phantom fabrication. Figures 3(a)-3(f) show the scanning electron microscope (SEM, Hitachi, SU8220) images of electrospun PLA fibers collected for cylinder rotation speeds ranging from 500 rpm to 3000 rpm. Fibers with the same orientation were obtained for a rotational speed of the cylinder over 2500 rpm.
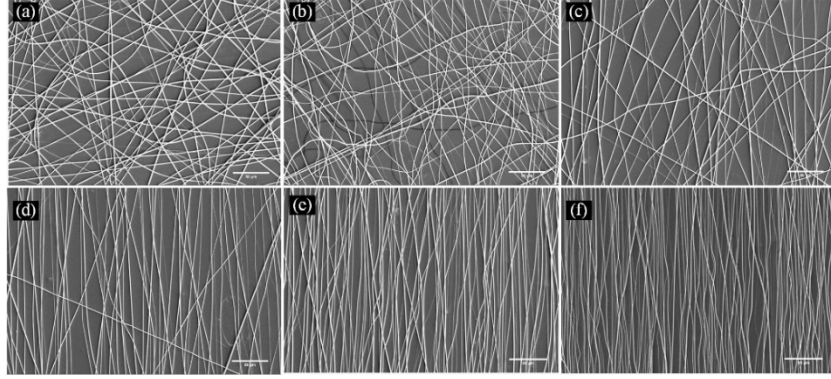

Fig. 3. SEM images of electrospun PLA fibers at different cylinder rotational speeds. (a) 500 rpm, (b) 1000 rpm, (c) 1500 rpm, (d) 2000 rpm, (e) 2500 rpm, (f) 3000 rpm. The scale bar is 50 μm.

3.2 Statistical analysis of electrospun PLA fibers

The distribution of fiber orientations in each sample is defined as the frequencies of all fibers aligning along the orientation angle θ ($0° < \theta \leq 180°$). This value is calculated based on a statistical analysis of 100 fibers randomly selected from the SEM images under 300 x magnification and displayed in a histogram for the full range of the orientation angle θ in steps of 10°. Figures 4(a)-4(f) show the histograms of the electrospun fibers collected at cylinder rotational speeds ranging from 500 rpm to 3000 rpm. Further quantitative analysis of the fibers orientations is given by calculating the standard deviation of their distribution:

$$\sigma = \sqrt{\sum_{i=1}^{18} n_i (\theta_i - \alpha)^2 \Big/ \sum_{i=1}^{18} n_i} \qquad (3)$$

where θ_i stands for the ith angle interval; α is the average orientation angle of all fibers, n_i is the number of fibers aligned along the ith angle.
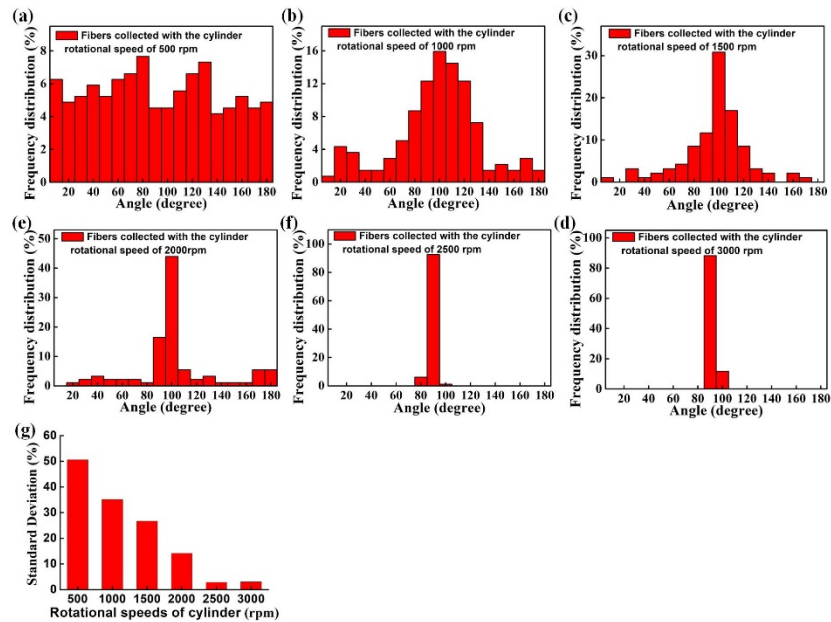
Fig. 4. Distribution of collecting electrospun fibers orientations for a cylinder rotational speed
of (a) 500 rpm, (b) 1000 rpm, (c) 1500 rpm, (d) 2000 rpm, (e) 2500 rpm, and (f) 3000 rpm. (g)
Standard deviation for the distribution of fibers as a function of cylinder rotational speed.

According to Fig. 4(g), the standard deviation for the distribution of fiber orientations
remains steadily lower than 3% for cylinder rotational speeds above 2500 rpm. The
histograms and standard deviation analyses show that the distribution of fiber orientations can
be effectively controlled by changing the cylinder rotational speed and that fibers with
uniformly distributed orientations can be obtained by increasing the cylinder rotational speed
above 2500 rpm. To further evaluate whether the cylinder rotational speed affect the size of
the produced fibers, 100 fibers were randomly selected from each SEM image and magnified
800 x for statistical analysis of the fibers diameters. According to Figs. 5(a)-5(e), the
diameters of the electrospun fibers mainly remain in the range of 1~2.2 µm at different
cylinder rotational speeds, indicating that the process of fiber collection has negligible effect
on the fiber size. The thicknesses of all the samples were measured using a BRUKER
DektakXT profilometer. The results show that the electrospun fibers form a film of the
identical thickness (5.3 ± 0.7 µm), regardless the difference in the rotational speed of the
cylindrical collector.
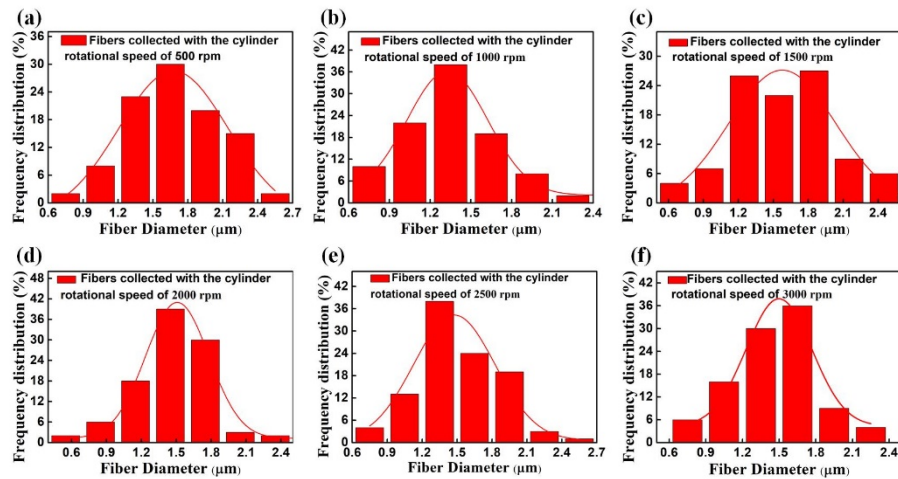
Fig. 5. Size distribution of the electrospun fibers collected for a cylinder rotational speed of: (a)500 rpm, (b)1000rpm, (c)1500rpm, (d)2000rpm, (e)2500rpm, and (f)3000 rpm.

3.3 Birefringence of the electrospun PLA fibers

We used a polarizing microscope (BX51, OLYMPUS) equipped with a 100-watt quartz halogen light source to detect the brightness fluctuations induced by the rotation of the birefringent sample [41]. A GigE CCD camera (DFK-23G274, Imaging Source Inc., Taipei, Taiwan) was used to image the field of view without sample in an orthogonal mode for three times, and the pixel information was extracted and converted to grayscale using ImageJ (ImageJ, US National Institutes of Health, MD, USA). The resulting mean value of the pixels is 0.015 ± 0.964. A double-sided tape was adhered onto the surfaces of coverslips pretreated with plasma into a hollow rectangular shape, and then aluminum foil with fibers were overridden on the coverslips. The samples of electrospun PLA fibers were finally transferred onto the coverslips in a lossless manner after removing the aluminum foil carefully. Three random regions of interest (ROIs) (630 μm × 350 μm) with the same β were imaged in an orthogonal mode for each sample, where the β was random selected for different samples. The deviation of the brightness intensity of ROIs was calculated by extracting a green channel of the highest sensitivity of the images using ImageJ and plotted using the Origin software package (Origin 2018, OriginLab Corp., MA, USA). As presented in Fig. 6(a), the deviations indicating the uniform distribution of fibers in each of the samples. To determine the relationship of brightness-to-orientation, the samples were imaged at individual rotation angles ranging from 5° to 355° in steps of 10° in an orthogonal mode. The mean brightness at each orientation was then obtained from the pixel values in the green channel of the highest sensitivity of the microscopic images using ImageJ and brightness-to-orientation function of the fibers was plotted using Origin software package. Figure 6(b) shows the brightness-to-orientation curves at different cylinder rotational speeds ranging from 500 to 3000 rpm. The light intensity I is periodic in β as expressed in Eq. (2), with maxima at $\beta = (2n + 1)\pi/4$ and minima at $\beta = 2n\pi/4$ (n = 0, 1, 2, 3). The light intensity increases as the rotational speed of the fiber collection cylinder increases, indicating the increased birefringence. These experimental results imply that electrospun fibers with different fiber orientation distributions can be effectively produced by changing the rotational speed of the fiber collection cylinder to simulate the polarization characteristics of different tissue types.
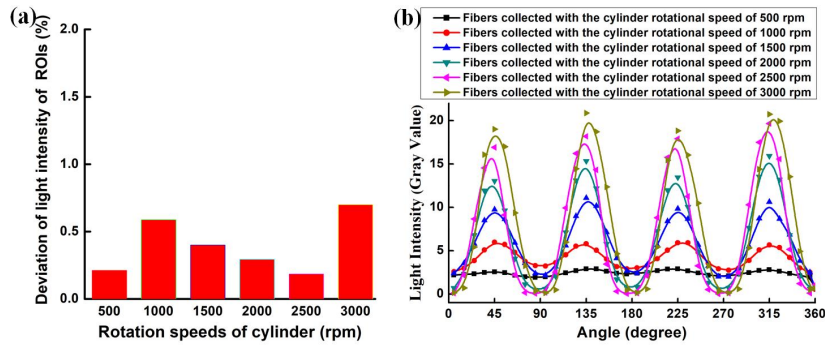
Fig. 6. Brightness of fibers at different positions. (a) Deviations of brightness of random ROIs in the same β on fibers collected with rotational speeds of cylinder from 500rpm to 3000rpm respectively. (b) Brightness-to-orientation curves of fibers collected with rotational speeds of cylinder from 500 rpm to 3000 rpm respectively.

3.4 Fabrication of the tissue-simulating phantoms

To produce multi-layered phantoms simulating different tissue polarization properties, PLA fibers were produced by the electrospinning process, collected on a collection cylinder at different rotational speeds ranging from 500 to 3000 rpm, flattened, and sandwiched between two PDMS layers. The two PDMS layers were prepared in advance by casting PDMS of 1.5 ml and 2.5 ml in a blank petri dish and a petri dish adhering with a cover glass, respectively. The sandwiched phantoms in a total thickness of 3 mm were produced by transferring the layer of electrospun fibers to a plasma-processed substrate of the grooved PDMS bottom layer and binding with the top PDMS layer. The purpose for grooving the substrate is to prevent complete embedment of the electrospun fiber layer within the PDMS layer. Figure 7 shows the electrospun fibers collected on the aluminum foil and the multilayered phantom embedded with the PLA fibers. The microscope image in Fig. 7(e) indicates that the tissue-simulating phantoms with embedded PLA fibers of designated orientations can be effectively produced without destruction of the fibers
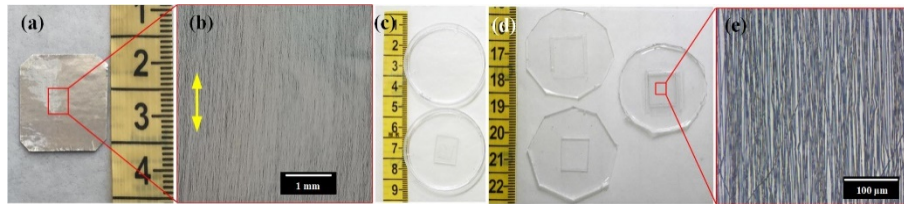

Fig. 7. Phantom fabrication process using precast PDMS layers and PLA fibers. (a-b) Fibers collected with the aluminum foil adhering to the cylinder. (c) Top: a blank petri dish is used for casting the PDMS top layer; bottom: a petri dish adhering with a rectangular cover glass (1 mm × 1 mm × 1.2 mm) is used for casting the grooved PDMS bottom layer. (d) Phantom fabricated by sandwiching the PLA fiber layer between the grooved PDMS bottom layer and the PDMS top layer. (e) Microscopic image of the produced phantom.

3.5 Polarization characteristics of phantoms and dense fibrous tissues

To facilitate quantitative comparison of polarization characteristics between phantoms, fibrous tissue of collagenous fibroma and healthy fibrous tissue, we derived the polarization ratio (POL) from the polarized microscopic images as [5]:

$$POL = \frac{I_{//} - I_{\perp}}{I_{//} + I_{\perp}} \tag{4}$$

where $I_{//}$ is mean brightness intensity of the sample when the analyzer is parallel to polarizer, and $I_\perp$ is the mean brightness intensity of sample when the analyzer is perpendicular to polarizer.

Figure 8 shows representative polarized images and the POL-to-orientation curves for the tissue-simulating phantoms as well as normal and fibroma dense connective tissue samples. The polarized microscopic images were acquired at rotation angles ranging from 0 ° to 360 ° in steps of 10 ° in both orthogonal and parallel mode. Phantom images from the green channel of the highest sensitivity and tissue images from the red channel of the highest sensitivity were extracted for the calculation of the mean brightness intensity at each fiber orientation. ImageJ (ImageJ, US National Institutes of Health, MD, USA) was used for image processing and the POL-to-orientation curves were plotted using the Origin software package (Origin 2018, OriginLab Corp., MA, USA).
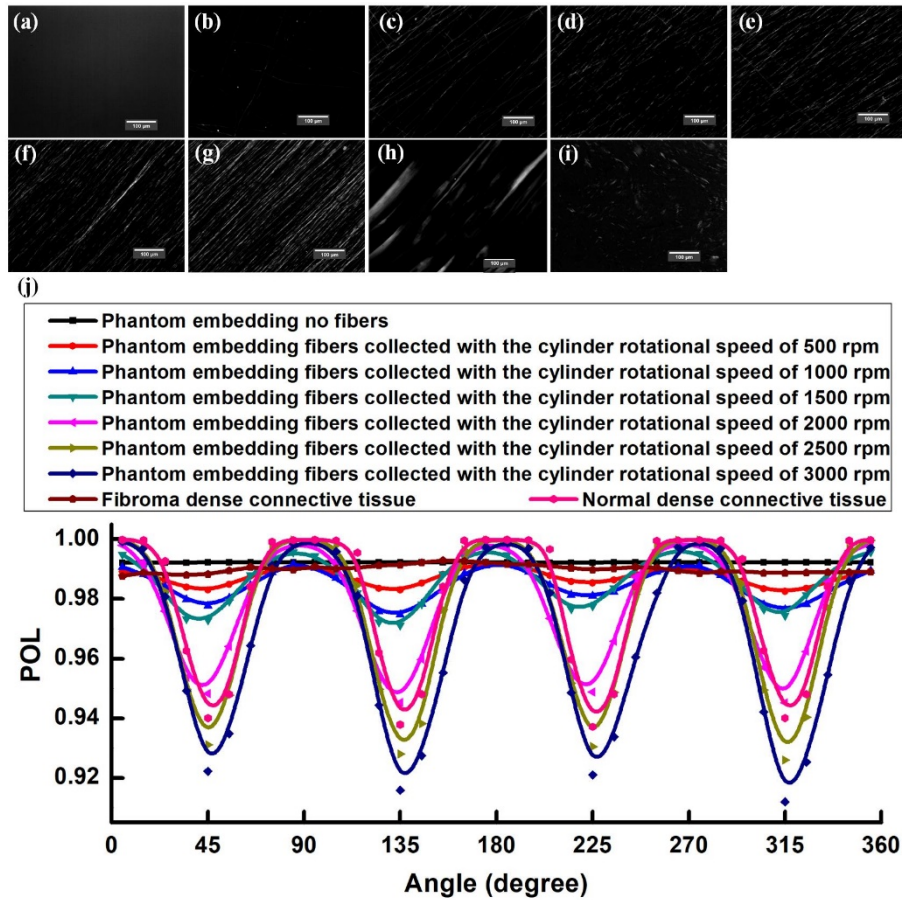

Fig. 8. Single-channel polarized microscopic images of: (a) the PDMS phantom without PLA fiber embedment; (b-g) PDMS phantoms embedding PLA fibers collected at different cylinder rotational speeds from 500 rpm to 3000 rpm respectively; (h-i) regular dense fibrous tissue and fibroma dense fibrous tissue. The above figures were taken at the β of π /4. (j) POL values vs. sample orientations for the produced phantoms, biopsies of normal and fibroma dense fibrous tissue.

To facilitate further assessment of sample polarization characteristics, the retardance parameter δ is derived from Eq. (2) at $\beta = (2n + 1)\pi/4$:

$$\delta = 2\arcsin\sqrt{I/I_1} \qquad (5)$$

where I_1 is the detected light intensity when the analyzer and polarizer aligned and I is the intensity of light intensity passing the analyzer. The retardance of the phantoms and the tissue samples were calculated based on the extracted mean brightness intensities of the microscopic images at null field and at $\beta = (2n + 1)\pi/4$. For each samples, the retardance value was averaged at four positions and listed in Table 1.

Table 1. The retardance levels for the phantoms, biopsies of dense fibrous tissue of collagenous fibroma and normal fibrous tissue at $\beta = (2n + 1)\,\pi\,/4$.

Sample	δ
Phantom embedding no fibers	0.125 ± 0.001
Phantom embedding fibers collected at the cylinder rotational speed of 500 rpm	0.145 ± 0.009
Dense fibrous tissue of collagenous fibroma	0.182 ± 0.007
Phantom embedding fibers collected at the cylinder rotational speed of 1000 rpm	0.213 ± 0.013
Phantom embedding fibers collected at the cylinder rotational speed of 1500 rpm	0.229 ± 0.012
Phantom embedding fibers collected at the cylinder rotational speed of 2000 rpm	0.332 ± 0.006
Normal dense fibrous tissue	0.357 ± 0.005
Phantom embedding fibers collected at the cylinder rotational speed of 2500 rpm	0.386 ± 0.007
Phantom embedding fibers collected at the cylinder rotational speed of 3000 rpm	0.417 ± 0.013

By comparing the polarized microscopic images of the phantoms in Figs. 8(a)-8(g), we observed that the phantom fiber orientation was correlated with the rotational speed of the collection cylinder in the electrospinning process. Such correlation was further confirmed by calculating POL and retardance levels at different rotational speeds, as shown in Fig. 8(j) and Table 1, respectively. Generally speaking, as the rotational speed increased from 500 rpm to 3000 rpm, the electrospun fibers were more orientated and the produced phantoms showed greater levels of polarization.

To further evaluate the biologic relevancy of the produced phantoms in light of the polarization characteristics, we also acquired the polarized microscopic images of the biopsy samples from both normal fibrous tissue and dense fibrous tissue of collagenous fibroma, as shown in Figs. 8(h)-8(i). According to this figure, normal fibrous tissue showed greater level of fiber orientation than that of collagenous fibroma, in coincidence with greater POL amplitudes as shown in Fig. 8(j). Moreover, Table 1 showed that the phantom retardance level ranged from 0.145 to 0.417 as the rotational speed of the collection cylinder varied from 500 to 3000 rpm. In comparison, the averaged retardance level of fibrous tissue ranged from 0.182 (for dense fibrous tissue of collagenous fibroma) to 0.357 (for normal dense fibrous tissue), indicating the technical feasibility of simulating tissue retardance by controlling the rotational speed and therefore fiber orientation distribution of the electrospinning process. In addition to fiber orientation distribution, other phantom parameters, such as the fiber size and the phantom thickness, also contribute to the polarization characteristics. More effective simulation of normal and disease tissue polarization properties requires further modeling and experimental efforts.

4. Discussion

The lack of suitable standard for calibration and validation has hindered the development and clinical deployment of many optical imaging devices, including polarized light imaging devices. In this study, we introduced a family of tissue-simulating phantoms that simulated the polarization characteristics of normal and abnormal fibrous tissue types. The phantoms were fabricated by binding a layer of electrospinning PLA fibers between two PDMS layers. The birefringence properties of the PLA fibers were adjusted by controlling the electrospinning process parameters. The polarization characteristics of the tissue-simulating phantoms were adjusted by controlling the orientation distributions of the collected PLA

fibers. Our experiments show that changing the rotational speed of the collection cylinder between 0 to 3000 rpm affected the orientation distribution of the PLA fibers and resulted in the designated POL levels resembling those of different fibrous tissue types, coincident with previous reports [13]. To evaluate the optical stability and repeatability of the produced phantoms, we prepared phantoms in six groups, where each group consists of three phantoms fabricated with fibers collected at the same rotation speed of cylinder. All the phantoms were tested on the 1th, the 15th, the 30th, and the 45th days in the same parameters after production of these phantoms. The tests yielded the retardance fluctuation of less than 5% for all the phantoms. Therefore, these solid phantoms have a long and stable shelf life, superior to similar phantoms made of liquid materials. We have previously produced multi-layered solid phantoms with embedded microfluidic channels and controlled absorption/scattering properties to simulate tissue vascular perfusion and metabolism [43,44]. We have also encapsulated hemoglobin in polymer microcarriers to simulate oxygenation dynamics of red blood cells [45]. It is technically feasible to integrate these techniques for reliable fabrication of multi-layered solid phantoms that simulate structural, optical and functional properties of normal and diseased tissues. These phantoms may find broad applications in medical device validation, calibration, disease diagnosis and treatment planning.

One limitation of this work is the lack of thickness control for the electrospun film. Accurate electrospinning of PLA film with more uniform thickness may be achieved by optimizing the design of the distributed electric field between the electrospinning nozzle and the collection cylinder. Another limitation is the narrow range of fiber sizes achievable by the electrospinning process. Our electrospun PLA fibers have a diameter between 1 to 2.2 µm, while histopathologic observations indicate that the diameter of tissue fibers ranges from 1 to 15 µm [46]. Future work should aim for electrospinning uniform birefringent PLA films with a wide range of fiber sizes and orientations to simulate different tissue conditions. In our current experiment, polarization images were acquired by a color CCD camera under broadband illumination and 8-bit images from a single color channel of the highest sensitivity were used for polarization analyses. The low bit depth and the broad illumination bandwidth are due to the limitations of the polarization microscope used in this study and represent the typical configurations of many clinically available polarized imaging devices such as a polarized dermoscope. For further quantitative analysis of birefringence and polarization characteristics of biologic tissues, a CCD camera with higher bit depth and a tunable light source with narrower bandwidth will be used. Since the scope of this reported work was to simulate polarization characteristics of fibrous tissues, transparent PDMS substrates were used for better visualization of embedded fiber alignments. In our future work, other ingredients, such as titanium dioxide, carbon black, and hemoglobin, may be mixed with the solid phantom to simulate scattering and absorption properties of various normal tissues and tissue malignancies.

5. Conclusion

We propose a novel phantom formulation to simulate polarization characteristics of fibrous tissues. PLA fibers with a diameter of 1~2.2 µm were produced by an electrospinning process and collected by aluminum foil adhering to a rotating cylinder. By controlling the speed of the rotating cylinder, we are able to control the orientation distribution of the PLA fibers, resulting in different polarization characteristics. By embedding electrospun PLA fibers of different orientation distributions between two PDMS layers, we are able to simulate the polarization characteristics of the dense fibrous tissue of collagenous fibroma and healthy skin. The polarization-mimicking phantoms are potential candidates for polarimetric medical devices calibration, medical training and tissue anomalies research.

Funding

References

1. E. Proksch, J. M. Brandner, and J. M. Jensen, "The skin: an indispensable barrier," Exp. Dermatol. **17**(12), 1063–1072 (2008).
2. L. Weil, *Crash Course: Quick Reference Guide to Medicine and Surgery-E-Book* (Elsevier Health Sciences, 2014).
3. C. D. Fletcher, *Diagnostic Histopathology of Tumors: 2-Volume Set with CD-ROMs* (Elsevier Health Sciences, 2007).
4. R. X. Xu and S. P. Povoski, "Diffuse optical imaging and spectroscopy for cancer," Expert Rev. Med. Devices **4**(1), 83–95 (2007).
5. S. L. Jacques, J. C. Ramella-Roman, and K. Lee, "Imaging skin pathology with polarized light," J. Biomed. Opt. **7**(3), 329–340 (2002).
6. R. R. Kulkarni, S. D. Sarvade, K. Boaz, S. N. Kp, and A. J. Lewis, "Polarizing and light microscopic analysis of mineralized components and stromal elements in fibrous ossifying lesions," J. Clin. Diagn. Res. **8**(6), ZC42–ZC45 (2014).
7. J. C. Ramella-Roman, K. Lee, S. A. Prahl, and S. L. Jacques, "Design, testing, and clinical studies of a handheld polarized light camera," J. Biomed. Opt. **9**(6), 1305–1310 (2004).
8. S. K. Manesh, C. L. Darling, and D. Fried, "Polarization-sensitive optical coherence tomography for the nondestructive assessment of the remineralization of dentin," J. Biomed. Opt. **14**(4), 044002 (2009).
9. D. Wang, Y. Chen, and J. T. Liu, "A liquid optical phantom with tissue-like heterogeneities for confocal microscopy," Biomed. Opt. Express **3**(12), 3153–3160 (2012).
10. R. X. Xu, D. W. Allen, J. Huang, S. Gnyawali, J. Melvin, H. Elgharably, G. Gordillo, K. Huang, V. Bergdall, M. Litorja, J. P. Rice, J. Hwang, and C. K. Sen, "Developing digital tissue phantoms for hyperspectral imaging of ischemic wounds," Biomed. Opt. Express **3**(6), 1433–1445 (2012).
11. S. Shen, H. Wang, Y. Xue, L. Yuan, X. Zhou, Z. Zhao, E. Dong, B. Liu, W. Liu, B. Cromeens, B. Adler, G. Besner, and R. X. Xu, "Freeform fabrication of tissue-simulating phantom for potential use of surgical planning in conjoined twins separation surgery," Sci. Rep. **7**(1), 11048 (2017).
12. O. N. Vassiliev, T. A. Wareing, J. McGhee, G. Failla, M. R. Salehpour, and F. Mourtada, "Validation of a new grid-based Boltzmann equation solver for dose calculation in radiotherapy with photon beams," Phys. Med. Biol. **55**(3), 581–598 (2010).
13. B. Liu, M. Harman, S. Giattina, D. L. Stamper, C. Demakis, M. Chilek, S. Raby, and M. E. Brezinski, "Characterizing of tissue microstructure with single-detector polarization-sensitive optical coherence tomography," Appl. Opt. **45**(18), 4464–4479 (2006).
14. M. Villiger, E. Z. Zhang, S. K. Nadkarni, W.-Y. Oh, B. J. Vakoc, and B. E. Bouma, "Spectral binning for mitigation of polarization mode dispersion artifacts in catheter-based optical frequency domain imaging," Opt. Express **21**(14), 16353–16369 (2013).
15. B. Baumann, S. O. Baumann, T. Konegger, M. Pircher, E. Götzinger, F. Schlanitz, C. Schütze, H. Sattmann, M. Litschauer, U. Schmidt-Erfurth, and C. K. Hitzenberger, "Polarization sensitive optical coherence tomography of melanin provides intrinsic contrast based on depolarization," Biomed. Opt. Express **3**(7), 1670–1683 (2012).
16. J. Xue, J. Xie, W. Liu, and Y. Xia, "Electrospun nanofibers: new concepts, materials, and applications," Acc. Chem. Res. **50**(8), 1976–1987 (2017).
17. B. Sundaray, V. Subramanian, T. Natarajan, R.-Z. Xiang, C.-C. Chang, and W.-S. Fann, "Electrospinning of continuous aligned polymer fibers," Appl. Phys. Lett. **84**(7), 1222–1224 (2004).
18. T. J. Sill and H. A. von Recum, "Electrospinning: applications in drug delivery and tissue engineering," Biomaterials **29**(13), 1989–2006 (2008).
19. R. Gopal, S. Kaur, Z. Ma, C. Chan, S. Ramakrishna, and T. Matsuura, "Electrospun nanofibrous filtration membrane," J. Membr. Sci. **281**(1-2), 581–586 (2006).
20. M. M. L. Arras, C. Grasl, H. Bergmeister, and H. Schima, "Electrospinning of aligned fibers with adjustable orientation using auxiliary electrodes," Sci. Technol. Adv. Mater. **13**(3), 035008 (2012).
21. M. V. Kakade, S. Givens, K. Gardner, K. H. Lee, D. B. Chase, and J. F. Rabolt, "Electric field induced orientation of polymer chains in macroscopically aligned electrospun polymer nanofibers," J. Am. Chem. Soc. **129**(10), 2777–2782 (2007).

22. X. Zong, K. Kim, D. Fang, S. Ran, B. S. Hsiao, and B. Chu, "Structure and process relationship of electrospun bioabsorbable nanofiber membranes," Polymer (Guildf.) **43**(16), 4403–4412 (2002).
23. S. F. Fennessey and R. J. Farris, "Fabrication of aligned and molecularly oriented electrospun polyacrylonitrile nanofibers and the mechanical behavior of their twisted yarns," Polymer (Guildf.) **45**(12), 4217–4225 (2004).
24. Z. Ma, Z. Hu, H. Zhang, M. Peng, X. He, Y. Li, Z. Yang, and J. Qiu, "Flexible and transparent optically anisotropic films based on oriented assembly of nanofibers," J. Mater. Chem. C Mater. Opt. Electron. Devices **4**(5), 1029–1038 (2016).
25. G. Mathew, J. Hong, J. Rhee, D. Leo, and C. Nah, "Preparation and anisotropic mechanical behavior of highly oriented electrospun poly (butylene terephthalate) fibers," J. Appl. Polym. Sci. **101**(3), 2017–2021 (2006).
26. I. Teh, F. L. Zhou, P. L. Hubbard Cristinacce, G. J. M. Parker, and J. E. Schneider, "Biomimetic phantom for cardiac diffusion MRI," J. Magn. Reson. Imaging **43**(3), 594–600 (2016).
27. W. Goth, B. Yang, J. Lesicko, A. Allen, M. S. Sacks, and J. W. Tunnell, "Polarized spatial frequency domain imaging of heart valve fiber structure," Proc SPIE Int Soc Opt Eng **9710**, 971019 (2016).
28. Y. Chen, J. Lin, Y. Fei, H. Wang, and W. Gao, "Preparation and characterization of electrospinning PLA/curcumin composite membranes," Fibers Polym. **11**(8), 1128–1131 (2010).
29. X. Ou and M. Cakmak, "Influence of biaxial stretching mode on the crystalline texture in polylactic acid films," Polymer (Guildf.) **49**(24), 5344–5352 (2008).
30. R. Y. Gu, K. L. Lurie, M. Pipes, and A. K. Ellerbee, "Variable-sized bar targets for characterizing three-dimensional resolution in OCT," Biomed. Opt. Express **3**(9), 2317–2325 (2012).
31. J. Doshi and D. H. Reneker, "Electrospinning process and applications of electrospun fibers," J. Electrost. **35**(2-3), 151–160 (1995).
32. H. Pan, L. Li, L. Hu, and X. Cui, "Continuous aligned polymer fibers produced by a modified electrospinning method," Polymer (Guildf.) **47**(14), 4901–4904 (2006).
33. Z.-M. Huang, Y.-Z. Zhang, M. Kotaki, and S. Ramakrishna, "A review on polymer nanofibers by electrospinning and their applications in nanocomposites," Compos. Sci. Technol. **63**(15), 2223–2253 (2003).
34. H. Fong, I. Chun, and D. Reneker, "Beaded nanofibers formed during electrospinning," Polymer (Guildf.) **40**(16), 4585–4592 (1999).
35. H. Liu and Y. L. Hsieh, "Ultrafine fibrous cellulose membranes from electrospinning of cellulose acetate," J. Polym. Sci., B, Polym. Phys. **40**(18), 2119–2129 (2002).
36. M. M. Demir, I. Yilgor, E. Yilgor, and B. Erman, "Electrospinning of polyurethane fibers," Polymer (Guildf.) **43**(11), 3303–3309 (2002).
37. W. Kaminsky, K. Claborn, and B. Kahr, "Polarimetric imaging of crystals," Chem. Soc. Rev. **33**(8), 514–525 (2004).
38. M. Born and E. Wolf, *Principles of Optics: Electromagnetic Theory of Propagation, Interference and Diffraction of Light* (Elsevier, 2013).
39. J. F. de Boer and T. E. Milner, "Review of polarization sensitive optical coherence tomography and Stokes vector determination," J. Biomed. Opt. **7**(3), 359–371 (2002).
40. E. Collett, *Field Guide to Polarization* (SPIE Press, 2005).
41. Z. Hu, Z. Ma, M. Peng, X. He, H. Zhang, Y. Li, and J. Qiu, "Composite film polarizer based on the oriented assembly of electrospun nanofibers," Nanotechnology **27**(13), 135301 (2016).
42. R. Oldenbourg, "Polarized light microscopy of spindles," Methods Cell Biol. **61**, 175–208 (1999).
43. Q. Wu, W. Ren, Z. Yu, E. Dong, S. Zhang, and R. X. Xu, "Microfabrication of polydimethylsiloxane phantoms to simulate tumor hypoxia and vascular anomaly," J. Biomed. Opt. **20**(12), 121308 (2015).
44. G. Liu, K. Huang, Q. Jia, S. Liu, S. Shen, J. Li, E. Dong, P. Lemaillet, D. W. Allen, and R. X. Xu, "Fabrication of a multilayer tissue-mimicking phantom with tunable optical properties to simulate vascular oxygenation and perfusion for optical imaging technology," Appl. Opt. **57**(23), 6772–6780 (2018).
45. G. Liu, Q. Wu, P. Dwivedi, C. Hu, Z. Zhu, S. Shen, J. Chu, G. Zhao, T. Si, and R. Xu, "Hemoglobin-Laden Microcapsules for Simulating Oxygen Dynamics of Biological Tissue," ACS Biomater. Sci. Eng. **4**(9), 3177–3184 (2018).
46. T. Ushiki, "Collagen fibers, reticular fibers and elastic fibers. A comprehensive understanding from a morphological viewpoint," Arch. Histol. Cytol. **65**(2), 109–126 (2002).